



Identification of wavemaker region in swirling flows using complex network analysis

Vivek T^{*}, Saarthak Gupta[†], Santosh Hemchandra[‡]

Precessing vortex core oscillation (PVC) is a self-excited flow oscillation observed in strongly swirled flows that show vortex breakdown. When these oscillations occur in technological applications such as combustor nozzles in gas turbines and aircraft engines, they can significantly alter combustor operation by impacting unsteady flame dynamics, fuel-air mixing and emissions. Prior work has shown that the PVC is caused by the precession of the vortex breakdown bubble (VBB). The flow region responsible for the generation of PVC oscillations is referred to as the wavemaker. Changes to the flow in the wavemaker region can induce or suppress the PVC oscillations. This region in the flow can be identified as the region where changes to the time-averaged mean flow have a large quantitative impact on the eigenvalue of the PVC mode (structural sensitivity) and can be derived from direct and adjoint linear stability analysis. This analysis while useful can realistically be performed in simple geometries that are axisymmetric or two-dimensional. Also, prior studies have shown that this approach requires accurately estimating time-averaged flow fields from CFD methods such as LES or RANS. In this paper, we present a data-driven approach using complex network theory to determine the shape and position of the wavemaker region associated with the PVC in a swirl nozzle using time series LES data. We present results from networks constructed using two measures of node connectivity that use correlation and mutual information between radial velocity fluctuations at various points in the flow field. The wavemaker is identified using points with high weighted closeness centrality. The results show that the wavemaker is positioned upstream of the breakdown bubble and extends into the swirl nozzle. These results agree well with the predicted position and extent of the wavemaker for the same flow configuration, obtained using structural sensitivity with mutual information giving a better match. The network analysis also shows that the wavemaker disappears when a centrebody is introduced due to the wavemaker region being disrupted. A windowed network analysis of the configuration with the centrebody shows an intermittent appearance and disappearance of the wavemaker region, coinciding with intermittent epochs of PVC oscillation. These results show that complex network analysis can be applied effectively to extract wavemaker information from time series data of turbulent fluid flows.

I. Introduction

Gas turbine combustors use swirled flows to promote fuel-air mixing and achieve reliable flame stabilization. At a sufficiently high intensity of swirl, a nominally axisymmetric central recirculation zone forms in the flow field. This is referred to as the vortex breakdown bubble (VBB) [1–3]. Several prior studies have shown that this flow can have a self-excited helical instability, referred to as the precessing vortex core (PVC) [3–6]. The PVC can significantly impact combustor operation by changing the macroscopic structure of the flame. This can in some cases lead to the emergence of undesirable thermoacoustic oscillations [7, 8]. On the contrary, other experimental studies [9, 10] show that the PVC oscillation can lead to the suppression of thermoacoustic oscillations. PVC can also promote rapid fuel-air mixing and reduce emissions of both NOX and carbon monoxide [11]. Therefore, understanding how the PVC can be passively controlled is a question of significant technological importance in developing gas turbine combustors.

Manoharan et al [6] performed a weakly non-linear asymptotic analysis of a swirled turbulent jet ($Re \sim 59000$) experiment wherein the level of the swirl was progressively increased. At the critical swirl number, vortex breakdown accompanied by a PVC emerges. This is consistent with earlier studies of variable swirl jets by Escudier et al [12]. The analysis showed that a marginally unstable helical mode appears with the onset of vortex breakdown, which induces precession of the VBB. Amplitude growth and saturation at a stable limit-cycle state then lead to the precession of the

^{*}MTech student, Dept. of Aerospace Engineering, Indian Institute of Science, Bengaluru

[†]PhD student, Dept. of Aerospace Engineering, Indian Institute of Science, Bengaluru, India, AIAA Student Member

[‡]Associate Professor, Dept. of Aerospace Engineering, Indian Institute of Science, Bengaluru, India, AIAA Member

axial vortex core around the bubble and induce a PVC in the flow. Several linear [13–16] and non-linear [6] analyses have shown that the *wavemaker* region driving the PVC is located at the upstream end of the VBB. Recent studies [14–17] show that changing the flow field structure in this region using a centrebody [14, 16, 17] at the upstream end of the VBB can suppress the PVC due to disruption of the wavemaker region. Therefore, in general, these studies suggest that identifying the wavemaker region for the PVC or other types of self-excited oscillation can inform minor design changes that can very effectively influence their limit cycle dynamics.

Gianetti and Luchini [18] showed that in the linear limit, self-excited flows have a region of high “structural sensitivity”, i.e., the region of flow where changes to the time-averaged flow result in a significant quantitative change in the eigenvalue of a self-excited hydrodynamic mode. Therefore, this region of structural sensitivity identifies the region of the flow that drives the self-excited oscillation, i.e., the wavemaker. This is identified from the spatial distribution of the instability mode amplitude and its adjoint [18]. Several recent studies have shown that linear stability analysis around time-averaged base flows determined from time-resolved LES and experimental data yields modes whose amplitude distributions compare closely with results for the same determined from the modal decomposition of the data directly [13–16, 19]. Wavemaker regions in these studies have been identified using spatial maps of structural sensitivity determined by the PVC mode and its adjoint [18]. The accuracy of this physics-based method requires accurate estimation of time-averaged flow field quantities with a sufficient spatial resolution that can be challenging to obtain experimentally and require long execution times for reliable statistical estimates if LES is used. Even so, in cases where the time-averaged flow doesn’t have any inherent geometric symmetries, a full three-dimensional stability analysis will be needed to identify the wavemaker. This is typically impractical, as the computational cost for these types of calculations can be comparable to an LES.

Therefore, in this paper, we assess the ability of data-driven approaches to identify wavemakers of global coherent flow oscillations using complex network representations of the flow. We focus on the PVC instability in the non-reacting flow in a swirl combustor that has been the subject of several past studies [8, 16, 17, 20]. We construct complex network representations whose nodes are points in space where velocity measurements are extracted from the LES. Internode edge connectivity strength is defined in two ways. This first approach uses correlation, as in prior studies — see for e.g., Krishnan et al [21]. The second approach uses the value of mutual information in velocity oscillations for a pair of nodes to determine connectivity. Hubs in these networks are identified using the edge connectivity strength weighted closeness centrality measure [22]. The nodes that constitute hubs are mapped back into physical space to identify the PVC wavemaker. Comparing the position and size of these regions with the physics-based result for the same flow from our earlier study [16] shows that the network approach does predict the wavemaker position with a remarkably good agreement with the corresponding physics-based linear stability analysis result. Thus, this result provides confidence that using the same complex network approach can reliably extract complex wavemaker information in other geometrically complex flows that would be challenging to analyze using physics-based linear stability methods.

II. Experimental Study

We briefly describe the experiment and setup that forms the basis for the study in this paper. We limit ourselves only to the details needed to understand this study while referring the reader to Gupta et al [17] for a more detailed description of the setup and measurement techniques. Figure 1 shows schematically, the single nozzle swirl combustor setup that forms the experimental basis for this study. Air is admitted into the combustor through a round duct of diameter $D = 38$ mm choked at the inlet as shown in Fig. 1. Swirl is induced in the flow by an axial swirler comprised of 8 flat blades set at an angle $\alpha_b = 45^\circ$ to the flow axis, yielding a geometric swirl number $S = 0.67$. The swirler is placed with its central hub 5.5 cm upstream of the dump plane. The swirling flow enters a cylindrical combustor with a

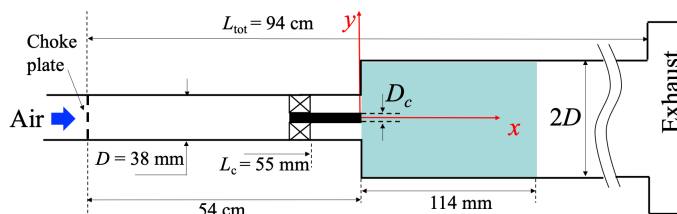


Fig. 1 Schematic of the single nozzle combustor facility, showing details of the centrebody and swirler [17].

Case	S	D_c	PVC oscillation
A	0.67	0 mm	coherent
B	0.67	9.5 mm	intermittent

Table 1 Centrebody geometry parameters investigated in this study. The value D_c is the diameter of the centrebody – see fig. 1. Adapted from Gupta et al [17].

diameter twice that of the duct. A fused silica quartz tube allowing for optical access is coaxially mounted and is used as the combustor section wall. The nominal flow Reynolds number is $Re = U_b D / \nu = 20,000$ where ν is the kinematic viscosity of air at $T = 300\text{ K}$ and $U_b = 8\text{ ms}^{-1}$ is the area averaged bulk flow velocity at the nozzle exit.

Stereoscopic PIV (sPIV) measurements as reported in Gupta et al [17] were performed to obtain three velocity components in a plane containing the nozzle centreline. The origin of coordinates in this study is positioned on the centreline at the dump plane, as shown in fig. 1. The y -axis is oriented along the laser sheet and the x -axis along the streamwise direction. The sPIV measurements were acquired over a window that encompasses the entire width of the combustor along the y direction and $3D$ along the streamwise direction. The field of view within the combustor test section is shown schematically by the green region in fig. 1. A total of 2048 sPIV images were acquired at an acquisition rate of 2 kHz. The laser diagnostics setup, data acquisition and PIV post-processing have been described in detail in the recent study of [17]. In this work, we have analyzed the non-reacting flow for a swirl number of $S = 0.67$ ($\alpha_b = 45^\circ$) in the absence of a centrebody.

Two cases from Gupta et al [17] are analyzed in this paper as shown in tab. 1. In case A, there is no centrebody in the nozzle ($D_c = 0$, see fig. 1) and in case B a centrebody with diameter $D_c = 9.5\text{ mm}$ is introduced. The length of the centrebody is chosen such that its end face is flush with the combustor dump plane. Table 1 also summarizes the PVC frequency and the state of the PVC observed in each case. Note that the centrebody causes the PVC to become intermittent, as was shown by combining wavelet and POD analysis by Gupta et al [17].

III. Large eddy simulation

This section summarizes key details of the LES study from Gupta et al [17] that forms the source of time-resolved computational data used in this work. We use explicit filtering LES (EFLES) to compute the non-linear time-resolved large-scale flow dynamics in this study. EFLES was proposed by Mathew and co-workers for non-reacting flows [23–25]. The spatially discretized governing equations of the flow are solved without any additional sub-grid scale modeling terms at every time step using an explicit Runge-Kutta method, followed by low pass filtering using a symmetric shift-invariant spatial filter with a high cutoff wavenumber [26]. This filtering operation models the transfer of turbulent flow kinetic energy from the smallest resolved scales on the LES mesh to the largest unresolved scales [24]. Our EFLES approach has been successfully used in prior studies for computing high Re non-reacting flows in swirl combustors different from that considered in the present study [15, 19]. We refer the reader to [27] for a detailed mathematical formulation of the EFLES method implemented in our flow solver.

We solve the fully compressible Navier-Stokes equations in strong conservation form on curvilinear structured multi-block meshes. An eighth-order central difference scheme is used for computing spatial derivatives and an explicit, third-order Runge-Kutta scheme [28] is used for time integration. A tenth-order, explicit filter is used to realize EFLES. To alleviate the complexity involved with mesh generation for complicated flow regions such as the region inside the swirler, overset mesh strategy is adopted. This approach allows us to decompose the entire flow domain into several overlapping subdomains, each of which is meshed using multi-block meshing. We use a trilinear interpolation scheme to interpolate the solution values at subdomain boundary points from the donor cells of the overlapping subdomain. The time marching is performed using a time step of $\Delta t = 1.75 \times 10^{-4}\text{ ms}$.

The fully three-dimensional computational domain (shown schematically in the transverse section) is shown in fig. 2. All boundary conditions are realized using the Navier-Stokes characteristic boundary conditions (NSCBC) approach [29]. Constant temperature no-slip boundary condition is specified on all the walls. A top-hat radial variation at the inlet boundary is imposed to match the mass flow rate in the experimental study. A constant temperature of 300.0 K is specified at the inlet and walls. At the non-reflecting outlet, we impose a reference pressure of 1 atm. The origin for the LES study is also positioned along the centreline at the dump plane, as shown in fig. 2.

The mean flow field quantities from LES are obtained by averaging over 1400 samples spanning 105 PVC oscillation cycles. The samples for averaging are collected after 0.25 domain flow-through times. This was sufficient to determine

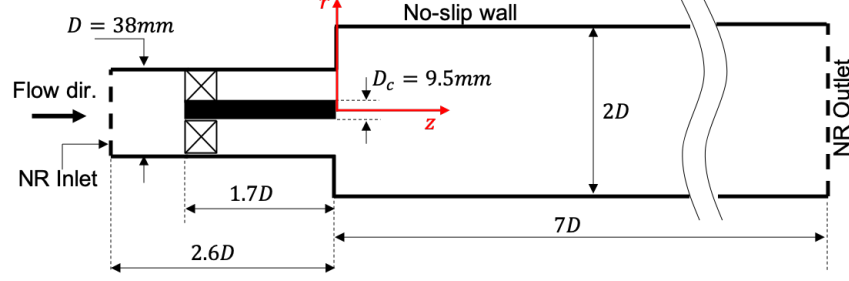


Fig. 2 Schematic of the LES computational domain geometry.

time-averaged flow statistics from the LES that agree well with sPIV measurements [16]. We also show in the same paper by comparing spectral POD [30] modes determined from sPIV experimental measurements and LES that, the large-scale dynamics of the PVC oscillation predicted by the LES agree well with the prediction from the sPIV measurements. For a detailed comparison of the LES and experimental data, we refer the reader to our prior paper [16].

For performing time-frequency and complex network analyses, time series signals are extracted from the LES data at discrete points, distributed between $r/D = \pm 1.0$ and $z/D = 0.0$ to 4.0 in a plane passing through the combustor axis. Time series data is also sampled on another set of discrete points, distributed between $r/D = \pm 0.5$ and $z/D = -1.0$ to 0.0 (inside the nozzle) in the same plane passing through the combustor axis. Note that this section of the flow field is optically inaccessible in the experiment [17]. These time series signals are extracted with a sampling rate of 20 kHz.

We characterize the global intermittency in the spatially integrated flow kinetic energy in the combustor using an intermittency factor, Γ , as follows [31],

$$\Gamma = \text{Prob}\{k(t) > k_{\text{thresh}}\} \quad (1)$$

where $k(t)$ corresponds to the time series of the spatially integrated kinetic energy over the plane that spans the combustor domain. The value of k_{thresh} is chosen to be 70% of the maximum $k(t)$ value in case A (see tab. 1). The intermittency factor, Γ thus, quantifies the probability that the flow is globally coherent. We obtain $\Gamma = 0.65$ for case A and $\Gamma = 0.22$ for case B. This large reduction in the value of Γ when a centrebody is introduced shows that the flow in case B has intermittent oscillations. This result is consistent with the observation made experimentally by Gupta et al. [17] where introduction of a centrebody results in an intermittent suppression of the PVC oscillation.

We apply wavelet-filtered POD (WPOD) described by Gupta et al [17] on the time-series data extracted from the LES to characterise the temporal variation of the amplitude of intermittent PVC oscillations in case B. This method yields a reconstruction of the flow dynamics in a specific frequency band of the following form,

$$\mathbf{q}(r, z, t) = \sum_{k=1}^{\infty} a_k(t) \hat{\mathbf{q}}_k(r, z) \quad (2)$$

where, $a_k(t)$ are temporal modal amplitude variations and $\hat{\mathbf{q}}_k(r, z)$ are WPOD modes that describe flow dynamics. This decomposition yields a spectrally resolved modal decomposition for flows that have oscillations that are globally spatially coherent but intermittent in time. Thus, the a_k in eq. 2 show non-stationary intermittent oscillation characteristics. As described in Gupta et al [17], time series data of flow field variables at every spatial point in the flow domain is projected into wavelet space using the continuous wavelet transform. The coefficients outside the frequency band containing PVC oscillations are set to zero and the inverse transform is applied to recover wavelet filtered flow snapshots in the time domain. The decomposition in eq. 2 is determined by performing a proper orthogonal decomposition (POD) of the wavelet filtered time series snapshots. Further details of this procedure and comparisons with POD and spectral POD can be found in Gupta et al [17].

IV. Hydrodynamic stability analysis

The wavemaker position for the coherent PVC in case A (see tab. 1) is obtained from linear global hydrodynamic stability analysis on the time averaged flow field from LES, as described in Gupta et al. [16]. The methods are summarized here for the readers' convenience. Linear stability analysis is performed in the cylindrical coordinate system (r, θ, z) (fig. 1) and assumes the time-averaged mean flow field to be axisymmetric. The instantaneous flow field

variables $\mathbf{q} = [u_r \ u_\theta \ u_z \ p]^T$ are decomposed using a triple decomposition ([32]) as into an axisymmetric time-averaged field ($\bar{\mathbf{Q}}$), a coherently oscillatory component (\mathbf{q}') and an incoherent turbulent component (\mathbf{q}''), as, $\mathbf{q} = \bar{\mathbf{Q}} + \mathbf{q}' + \mathbf{q}''$. Using the above decomposition in the governing equations and phase averaging, yields the linearized Navier-Stokes equations for (\mathbf{q}') as follows [6],

$$\mathcal{B} \frac{\partial \mathbf{q}'}{\partial t} + \mathcal{L}\{\bar{\mathbf{Q}}\} \mathbf{q}' = 0 \quad (3)$$

where, $\mathcal{B} = \text{diag}(1, 1, 1, 0)$ and $\mathcal{L}\{\bar{\mathbf{Q}}\}$ is a linear operator arising from spatial derivative terms associated with the advection of perturbations by the time averaged flow, turbulent transport and viscous terms. We use the Newtonian eddy viscosity hypothesis with a spatially varying eddy viscosity, ν_T , to model the term corresponding to turbulent transport of coherently fluctuating momentum in $\mathcal{L}\{\bar{\mathbf{Q}}\}$. At every spatial location, ν_T is determined by the time averaged flow momentum balance in a least-squares sense [6].

Introducing the normal mode form: $\mathbf{q}'(r, \theta, z, t) = \tilde{\mathbf{q}}_m(r, z) \exp[i(m\theta - \omega t)]$ in eq. 3 yields,

$$-i\omega \mathcal{B} \tilde{\mathbf{q}}_m + \mathcal{L}_m\{\bar{\mathbf{Q}}\} \tilde{\mathbf{q}}_m = 0 \quad (4)$$

where, the operator \mathcal{L}_m is obtained by setting $\frac{\partial}{\partial \theta} \rightarrow im$ in \mathcal{L} . Along with appropriate boundary conditions, eq. 4 yields an eigenvalue problem for the global eigenvalue ω and the associated eigenmode, $\tilde{\mathbf{q}}_m$. This is solved numerically using the finite-element method. The variational form of eq. 4 that includes appropriate boundary conditions is derived and then spatially discretized on an unstructured mesh composed of triangular elements. Velocity and pressure perturbation fields are discretized using P2 and P1 Taylor-Hood finite elements, respectively. Projecting the variational form onto a subspace spanned by the same finite-element basis for velocity and pressure (Galerkin method), yields the matrix eigenvalue problem representing the discretized version of eq. 4 [15, 16],

$$A \tilde{\mathbf{q}}_{m,d} = \omega B \tilde{\mathbf{q}}_{m,d} \quad (5)$$

where, $\tilde{\mathbf{q}}_{m,d}$ is the eigenmode discretized at collocation points on the mesh and the A and B matrices are the discrete equivalents of operators \mathcal{L}_m and \mathcal{B} in eq. 4, respectively. The FreeFEM++ software suite is used to obtain these discretized system matrices [33] and the eigenvalue solutions are computed using the MATLAB *eigs* function.

The wavemaker for the PVC mode determined from the solution of eq. 5, is then determined from its local structural sensitivity, i.e., how large the drift in the eigenvalue is for a fixed change in the time averaged flow field at a single point. Following the analysis of Gianetti and Luchini [18], the upper bound on this drift at a given mesh point ' k ' is given by [18, 34],

$$s_k = \frac{||\mathcal{B} \tilde{\mathbf{q}}_{m,k}^\dagger|| ||\mathcal{B} \tilde{\mathbf{q}}_{m,k}||}{|\langle \tilde{\mathbf{q}}_{m,d}^\dagger, B \tilde{\mathbf{q}}_{m,d} \rangle|} \quad (6)$$

where $\tilde{\mathbf{q}}_{m,d}^\dagger$ is the adjoint mode associated with the PVC mode, $\tilde{\mathbf{q}}_{m,d}$. The terms in the numerator of eq. 6 are simply the components of these modes at mesh point ' k '. The adjoint mode $\tilde{\mathbf{q}}_{m,d}^\dagger$ is determined using the discrete adjoint approach that involves taking the conjugate transpose of eq. 5 [16, 34]. The spatial region with large nonzero values of s_k for the coherent self-excited PVC mode then identifies its *wavemaker* [18].

Figure 3 shows the unstructured mesh used for the linear stability analysis of case A (tab. 1). We impose a homogeneous Dirichlet condition for the velocity components at the upstream end ($z/D = -0.6$). No-slip and no-penetration conditions are imposed on the walls. At the downstream boundary ($z/D = 4.0$), a traction-free boundary condition is applied. This imposes a zero fluctuating traction force, which allows the velocity and pressure values at the boundary to float.

The analysis described in this section to determine the wavemaker is tractable at a realistic computational cost due to the fact that the asymmetry of the base flow allows for a large reduction in the eventual size of the eigenvalue problem in eq. 5. However, practical industrial flows feature flow configurations for which these types of assumptions are not possible, e.g., flows from multiple closely spaced micromix swirl nozzles proposed for use in gas turbine combustors burning hydrogen. Therefore, we evaluate an alternative data-driven method that uses ideas from complex network theory to identify wavemakers. The aim here is to compare predictions of the wavemaker determined from the physics based LSA approach described in this section and in Gupta et al [16] with that from complex network analysis.

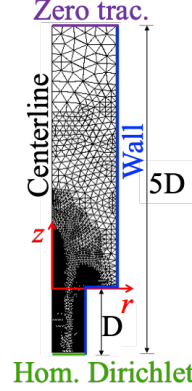


Fig. 3 Schematic of the axisymmetric domain used for the linear stability analysis. The unstructured mesh qualitatively illustrates the spatial point distribution for the hydrodynamic stability computations.

V. Complex network analysis

The turbulent swirl nozzle combustor flow fields associated with cases A and B (tab. 1) are viewed as complex systems. Complex network analysis aids in uncovering critical regions in such systems that govern the emergent ordered behavior of these systems [35, 36]. Thus, the PVC oscillation cases A and B represent emergent phenomena arising from complex system dynamics. The complex networks analyzed in this study can be mathematically represented as an ordered pair

$$\mathbf{G} = (\mathbf{V}, \mathbf{E}) \quad (7)$$

where \mathbf{G} is the network, consisting of a set of nodes \mathbf{V} and a set of weighted edges \mathbf{E} connecting these nodes. Every element of the set $e_k \in \mathbf{E}$ is an unordered set of the form $e_k = \{\{v_i, v_j\}, w_k\}$ that denotes the existence of non-trivial interconnection with weight w_k , between the nodes $v_i, v_j \in \mathbf{V}$ [37]. We do not associate directivity with edges in the work presented in this paper.

We construct networks associated with the flow fields in cases A and B using time series data extracted from the LES at discrete grid points on which the LES is monitored, as described in section III. Additionally, we also construct networks using the data obtained from the prior experimental study [17] on the sPIV grid. The grid points in each case therefore comprise members of the set \mathbf{V} in eq. 7, i.e. the nodes of the network. We establish edges between nodes and their weights, w_k using numerical values of two different statistical measures of interdependence: (i) Pearson's correlation coefficient, and (ii) average mutual information [38]. These are computed using time series data of the radial velocity component (u_r) of the flow. In this paper, we compute the correlation and mutual information between a pair of nodes as follows. Let $u_{r,i}$ and $u_{r,j}$ be the radial component of velocity at nodes i and j respectively. We can consider their corresponding time series as the realizations of two discrete random variables. The Pearson's correlation coefficient (\mathbf{R}_{ij}) between the two random variables, $u_{r,i}(t_k)$ and $u_{r,j}(t_k)$ for $k \in \{1, 2, \dots, N\}$ is computed using the following expression

$$\mathbf{R}_{ij} = \frac{\sum_{k=1}^N (u_{r,i}(t_k) - \langle u_{r,i} \rangle) (u_{r,j}(t_k) - \langle u_{r,j} \rangle)}{\sqrt{\sum_{k=1}^N (u_{r,i}(t_k) - \langle u_{r,i} \rangle)^2} \sqrt{\sum_{k=1}^N (u_{r,j}(t_k) - \langle u_{r,j} \rangle)^2}} \quad (8)$$

where, $\langle u_{r,i} \rangle$ and $\langle u_{r,j} \rangle$ denotes the temporal mean of $u_{r,i}$ and $u_{r,j}$ respectively across N realizations.

The mutual information quantifies the information content shared between the two discrete random variables and is defined as,

$$\mathbf{M}_{ij} = \sum_{\substack{\tilde{u}_{r,i} \in u_{r,i}, \\ \tilde{u}_{r,j} \in u_{r,j}}} p(\tilde{u}_{r,i}, \tilde{u}_{r,j}) \log_2 \left(\frac{p(\tilde{u}_{r,i}, \tilde{u}_{r,j})}{p(\tilde{u}_{r,i})p(\tilde{u}_{r,j})} \right) \quad (9)$$

where $p(u_{r,i})$ and $p(u_{r,j})$ correspond to marginal probability distributions for $u_{r,i}$ and $u_{r,j}$ respectively, and

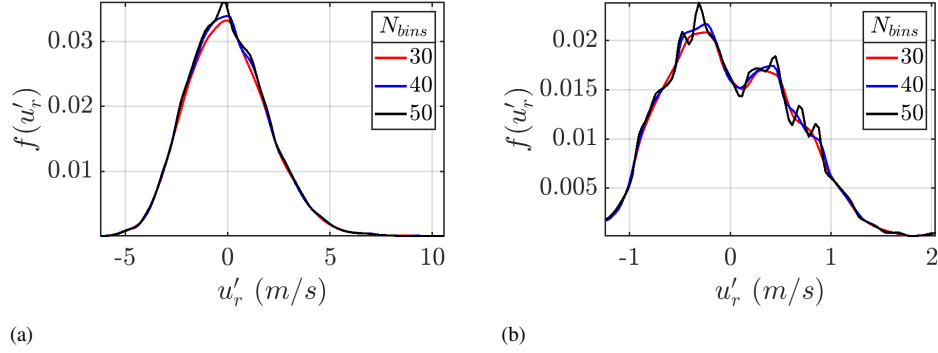


Fig. 4 Probability distribution of fluctuating the radial velocity component, $f(u'_r)$, from case B for three different numbers of bins N_{bins} at (a) $r/D = 0.2$, $z/D = 0$ and (b) $r/D = 0.48$, $z/D = 2.46$.

$p(u_{r,i}, u_{r,j})$ is their joint probability distribution. Equation 9 can be rewritten as follows,

$$\mathbf{M}_{ij} = H(u_{r,i}) - H(u_{r,i} | u_{r,j}) \quad (10)$$

$$= H(u_{r,i}) + H(u_{r,j}) - H(u_{r,i}, u_{r,j}) \quad (11)$$

where, $H(u_r)$ is the Shannon entropy [39] associated with u_r , computed from its probability density function, as follows,

$$H(u_r) = - \sum_{\tilde{u}_r \in u_r} p(\tilde{u}_r) \log_2 p(\tilde{u}_r) \quad (12)$$

When defined this way, the units of entropy, $H(u_r)$, is referred to as ‘bits’. The entropy quantifies the average uncertainty associated with the random variable u_r . Thus, mutual information can be interpreted in two ways based on expressions in eqs. 10 and 11. Equation 10 suggests that \mathbf{M}_{ij} is the amount of information acquired from $u_{r,j}$ that reduces the uncertainty of $u_{r,i}$, or vice versa [38]. Equation 11 interprets \mathbf{M}_{ij} as the excess number of bits that would be required to describe the information associated with $u_{r,i}$ and $u_{r,j}$ by ignoring their coupled behavior and treating them to be two independent random variables.

From eq. 11, one can infer that mutual information is a symmetric measure. For this reason, while mutual information does quantify the causal link between two random variables, it cannot determine the directivity of causality. However, unlike the implicit presumption of a linear relationship between two random variables when computing Pearson’s correlation coefficient, no such assumption is made when defining mutual information as it is based on the full joint probability distribution of the two random variables involved. As such, this doesn’t make any assumption as to the true nature of the coupling between the random variables. This makes mutual information a more precise measure of causality when the relationship between the two random variables involved can in general be non-linear [40, 41].

We use the non-parametric histogram binning approach on data to construct the various probability distributions in eq. 10 from time series u_r data extracted from LES of cases A and B in tab. 1 [42]. This approach is extensively used and incurs minimal computational complexity. We adapt this method in the present study, with each bin having a uniform width. The width of the bins has to be chosen in such a way that the effect of random fluctuations is ignored, while it retains the major features and patterns exhibited by the data distribution. This consideration of bias-variance trade-off results in an optimal choice of bin width. Figure 4a-b show typical probability distributions of u_r at $(r/D, z/D)$ of (0.2,0) and (0.48,2.46) from data extracted from case A for three different numbers of bins, $N_{bins} = 30, 40$ and 50 . Based on these results and at other points in the flow domain, $N_{bins} = 40$ was chosen to construct all probability distributions needed for mutual information calculations in this paper.

The need to resolve the dynamics of the smallest significant spatial scales in the flow leads to large networks with a substantial number of nodes. Accordingly, sparsification is performed to reduce the computational cost associated with the determination of critical regions in the network. In this paper, sparsification is achieved by thresholding the weight w_k associated with edges in the network as follows. A pair of nodes share an edge only if the edge weight exceeds a threshold value when determined using either Pearson’s correlation or mutual information. The choice of threshold value in each case is chosen such that a statistically significant number of connections that preserve essential network structures are retained. We ensure this in the present paper by requiring that the final sparsified network is fully

connected, i.e., at every node, there is at least one connection to one other node in the network. The preservation of edge density makes for common ground when comparing two networks with different edge criteria.

The weighted adjacency matrix, $\mathbb{A}_{ij,w}$ is computed to represent the connectivity between two nodes of the network, as follows,

$$\mathbb{A}_{ij,w} = |\mathbf{C}_{ij}| \{ \Theta(\mathbf{C}_{ij} - \mathbf{C}_{th}) - \delta_{ij} \} \quad (13)$$

where, $\mathbf{C}_{ij} = \mathbf{R}_{ij}$ or \mathbf{M}_{ij} , \mathbf{C}_{th} is the threshold chosen, $\Theta(x)$ is the Heaviside function, δ_{ij} is the Kronecker delta. Equation 13 ensures that nodes i and j are connected if the magnitude of $\mathbf{C}_{ij} > \mathbf{C}_{th}$. Thus, $\mathbb{A}_{ij,w}$ now determines the set \mathbf{E} in eq. 7 and thereby, the structure of the network representing the interaction between flow oscillations at various points.

The wavemaker in the flow is determined by identifying critical regions or hubs in the complex network. We use the weighted closeness centrality measure, \mathbb{C}_i , to identify hubs in the network. The definition of \mathbb{C}_i is as follows [22],

$$\mathbb{C}_i = \sum_{j=1, j \neq i}^N 2^{-d_{ij}} \quad (14)$$

where, d_{ij} represents the least costly path between nodes i and j and is determined using Dijkstra's algorithm as follows,

$$d_{ij} = \min \left(\frac{1}{\mathbb{A}_{ih}} + \frac{1}{\mathbb{A}_{hk}} + \dots + \frac{1}{\mathbb{A}_{rs}} + \frac{1}{\mathbb{A}_{sj}} \right) \quad (15)$$

where, $i - h - k - \dots - r - s - j$ represents a path from a set of all possible paths connecting the nodes i and j . The value of d_{ij} corresponds to the path, which minimizes the summation in eq. 15. The negative sign of the exponent in eq. 14 shows that a large value of \mathbb{C}_i will result if a node i is connected to many other nodes in the network via low-cost paths. A cluster of nodes with high \mathbb{C}_i when mapped back into physical space, identify the critical region in the flow. Since by construction, flow oscillations in the critical region are well-correlated or share significant information with flow oscillations at all other points in the network, this region represents the wavemaker of the emergent oscillatory behavior in the flow. As presented, the analysis method described above makes no assumptions about symmetries in the flow and is easily extended to fully three-dimensional flows in complex geometries. Therefore, it is interesting to compare the position and extent of the wavemaker identified by complex network analysis in the flow with that from physics-based linear stability analysis for the present flow cases in tab. 1. These results will be discussed next.

VI. Results and discussion

Comparisons between PIV and LES predictions of time-averaged radial profiles of mean and RMS flow profiles, PVC modes obtained from SPOD and WPOD decompositions of the LES data, etc. are discussed in detail by Gupta et al [16]. These results show that flow field statistics, PVC modal energy, and PVC mode shape predicted by the LES agree well with the results obtained from sPIV measurements. Therefore, the LES results for cases A and B in tab. 1 are reliable numerical analogs of the experiment in Gupta et al [17]. For readers' convenience, we summarize key results concerning the PVC wavemaker from physics-based linear stability analysis for case A.

Figure 5a shows the eigenvalue spectrum for helical ($m = 1$) modes determined using LSA. The arrow in fig.5a points to the marginally stable eigenvalue associated with the VBB precession mode that is the cause of the PVC. The frequency of this mode, $f = 123$ Hz ($\omega = 3.83$) is in good agreement (to within 4%) with the experimental result for case A [17] marked by the blue solid vertical line in fig. 5a. Figure 5b shows the spatial distribution of the real part of the eigenmode component, \tilde{u}_r for the marginally stable eigenvalue. The black dashed curve corresponds to $\bar{U}_z = 0$ and demarcates the time-averaged VBB. We will use this approach to show the VBB shape in the rest of this paper. The spatial distribution of \tilde{u}_r indicates that this eigenmode is characterized by strong u_r fluctuations on the flow centreline due to the precession of the VBB. Note also that these centreline flow oscillations extend into the nozzle upstream of the dump plane. Figure 5c shows the structural sensitivity (S_k) map for this mode evaluated from eq. 6. The solid green curve ($\bar{U}_z = 0$) shows the time-averaged VBB. The S_k field shows that the wavemaker of the PVC mode lies a little upstream of the VBB on the centreline and extends into the nozzle. As discussed in Gupta et al [16], this result shows that the introduction of a centreboby in case A results in PVC suppression. This is because the wake recirculation zone behind the centreboby end face modifies the time-averaged flow and thus internal feedback within the flow that drives the PVC.

We next present the results from complex network analysis (CNA) applied to time series data extracted from LES for the cases in tab. 1. We construct the networks for both cases in tab. 1 using the methods described in section V. The

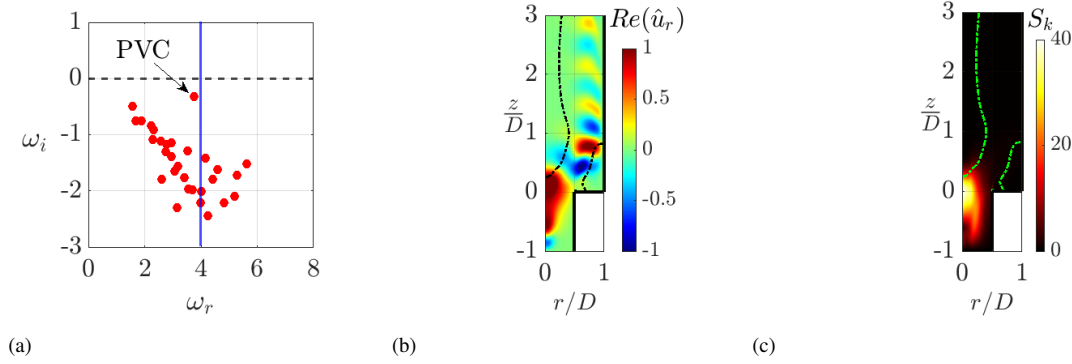


Fig. 5 (a) Eigenvalue spectra for helical ($m = 1$) modes. The arrow points to the marginally stable VBB precession mode. The blue solid line indicates the PVC frequency obtained from SPOD on the experimental data. (b) Radial component (\hat{u}_r) of the normalized eigenvector of the VBB precession mode. (c) Structural sensitivity map for the VBB precession mode. These results have been adapted from Gupta et al [16].

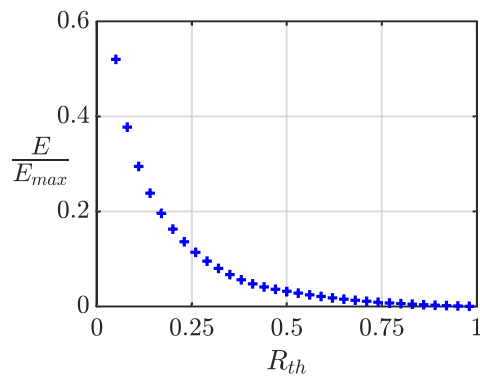


Fig. 6 Network edge density (E/E_{max}) variation with threshold R_{th} of correlation network for case A.

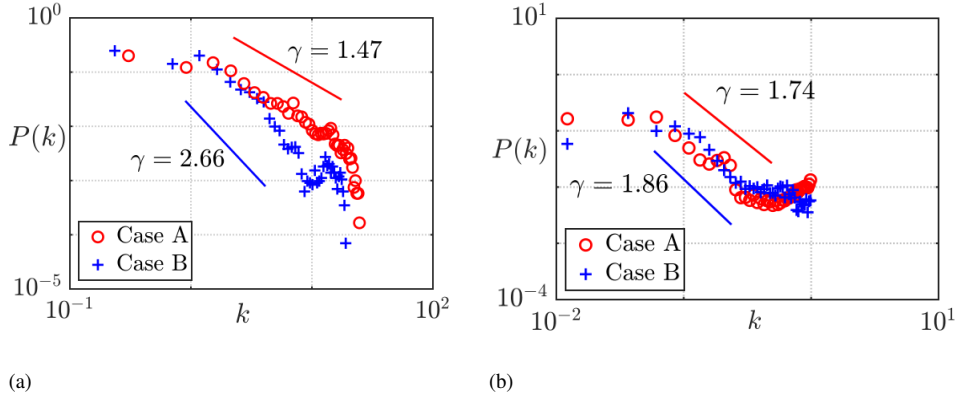


Fig. 7 Weighted degree distribution for networks obtained from case A and B in tab. 1 using (a) mutual information and (b) correlation

threshold C_{th} in eq. 13 when using correlation and mutual information to determine internode connectivity strength are 0.6 and 0.4 respectively. Figure 6 shows the variation of edge density for the network determined for case A as a function of C_{th} for the correlation network. Edge density (E/E_{max}) is the ratio of the number of edges in the network to the maximum possible number of edges. The rapid rise of E/E_{max} for $C_{th} < 0.6$ suggests the accumulation of numerous potentially spurious links with low values of $A_{ij,w}$ at these low threshold values. These insignificant edges make the degree distribution more uniform, and that in turn culminates in an inferior network structure that hinders its interpretability. Hence, $C_{th} = 0.6$ serves as a judicious choice for the correlation network. A similar analysis is used to determine the threshold of the mutual information network.

Figure 7a-b shows the variation of the probability distribution, $P(k)$, of weighted node degree k for mutual information and correlation-based networks, respectively. The weighted degree k of a node is the sum of the weights of the edges that the node is connected to. We determine $P(k)$ from the histogram of k computed with 40 bins. Figure 7a-b show that $P(k) \sim k^{-\gamma}$ with $\gamma > 0$. Networks constructed for systems with either weak or no coherent orderly dynamics, such as in case B (scale-free networks), typically have the power-law exponent (γ) lying in the range $2 < \gamma < 3$ [43]. Systems with coherent orderly dynamics have clusters of nodes, referred to as hubs, that are connected to surrounding nodes leading to several edges with high weighted degree. This results in a slower roll-off of $P(k)$ with k when compared to scale-free networks. Figure 7a shows that for case B, the network constructed with mutual information has $\gamma = 2.66$ showing scale-free behavior while $\gamma = 1.47$ in case A shows the emergence of hubs due to higher $P(k)$ values relative to case B for $k > 8$ [44]. The corresponding results for the network constructed using correlation (eq. 8) are shown in fig. 7b. Here, the marginal decrease in the value of γ from 1.86 for case B to 1.74 for case A suggests that both networks have similar characteristics and are not scale-free. This is inconsistent with the LES and experiment for case A. These results suggest that mutual information (eq. 10) quantifies causal links between spatial points more accurately than correlation (eq. 8). Mutual information, being a function of the joint pdf of velocity fluctuations on pairs of nodes, naturally captures causality between flow oscillations at these nodes, even when the underlying relationship between flow oscillations at the nodes is non-linear, as is the case in general, in turbulent unsteady flows. Correlation-based analysis, by its inherent assumption of linearity, demonstrably misrepresents causal relationships in instances where such relationships are non-linear.

The spatial extent and position of the wavemaker region are determined by hubs in the network. These hubs are identified using the spatial distribution of the weighted closeness centrality (WCC) measure. Figure 8a-b shows the spatial distribution of normalized WCC for networks corresponding to case A. The normalization factor employed for each result is the maximum observed value of the WCC metric within that specific result. Both fig. 8a-b show the presence of a hub at the dump plane on the nozzle axis. The result using mutual information in fig. 8a shows a spatially compact hub region when compared to the result from the network constructed using correlation. This result again suggests that mutual information is a better metric than correlation in pinpointing inter-nodal causal links. The high values of WCC in the hub show that these nodes are connected to other network nodes by several paths that have high weight (eqs. 14 and 15). In the case of the network constructed using mutual information, this implies that nodes in the hub have strong causal links with other nodes in the network. For this reason, they identify the wavemaker region in

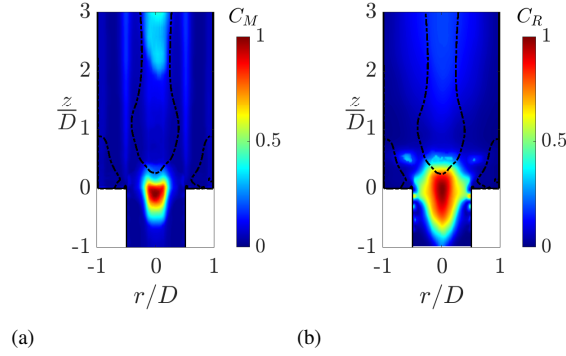


Fig. 8 Normalized weighted closeness centrality (C_i) computed using (a) mutual information with $M_{th} = 0.4$ (b) linear correlation with $R_{th} = 0.6$ on the transverse (radial) velocity time series data extracted from LES.

the flow, i.e., the region that drives the emergent coherent dynamics. Additionally, a relatively weaker and spatially non-compact hub can be seen at $z/D > 2$ in fig. 8a. This hub is possibly a signature of a chaotic attractor in the turbulent flow downstream of the VBB region, and its study is not the subject of this work. However, note that it is absent in the network determined from correlation, as fig. 8b shows. This result suggests further, that mutual information is a superior metric for identifying causal links between flow oscillations at various points in an unsteady flow.

We note that in recent studies that have applied complex network analysis to understand flow dynamics in reacting turbulent swirling flows using correlation to define internode connectivity with experimental data, results similar to those shown in fig. 8b are obtained [10, 19]. Note that in the fig. 8b, a small island of relatively high WCC at $\sim (\pm 0.5, 0.5)D$ is observed. This feature is absent from the result obtained using the network constructed using mutual information — see fig. 8a. This suggests that hypotheses of potential non-linear interaction between the breakdown bubble and the shear layer, due to the presence of these islands, may be unnecessary as these features may be a result of incorrect assignment of internode links based on correlation. This must, however, be verified by future work using other measures of causality, e.g., transfer entropy [45].

Figure 9a-b compares the wavemaker regions identified using WCC for networks constructed using mutual information and correlation respectively (left half) with the similar result determined from structural sensitivity (S_k) (fig. 5c) for case A in tab. 1. Figure 9a shows that the predicted wavemaker position and spatial extent from complex network analysis using mutual information closely match the result from structural sensitivity analysis. The result from the complex network constructed using correlation yields a wavemaker that is larger in spatial extent when compared to the structural sensitivity result. This result, along with others discussed in preceding paragraphs shows that mutual information in general, yields a better match with the unsteady characteristics of the system when compared to correlation. Therefore, we show results from network analysis for the mutual information based network construction method alone in the rest of this paper. In the interest of clarity, we will refer to these networks as mutual information (MI) networks.

Figure 10a-b compares the spatial WCC maps computed from MI networks for cases A and B. The WCC value has been normalized in each figure by its maximum value in each of the cases. The spatial distribution of WCC for case B (fig. 10b) shows that the region of strong WCC at the dump plane has all but disappeared, showing the absence of a hub in this network. This result is consistent with fig. 7a which shows that the MI network in this case, which has no PVC, is scale-free. Therefore, the result in fig. 10a-b suggests that the introduction of a centrebody in case B suppresses the PVC oscillation due to the disruption of the hub in the nominal case A. This result verifies the interpretation of the structural sensitivity map from linear theory and the mechanism of PVC suppression in Gupta et al [17]. *Prima facie*, the result in fig. 10a-b is the result of a network analysis that makes no assumptions of linearity of flow dynamics at any point. The structural sensitivity map from linear stability analysis in fig. 9a which at first glance appears to not leave out all non-linear dynamics, does so through turbulent momentum transport of coherent fluctuating momentum term. As such, the agreement with the network analysis wavemaker result in fig. 9a suggests that the eddy viscosity model formulated in Gupta et al [16] that models this process linearly, is essentially a reasonable leading order approximation to the influence of turbulent transport on the stability of the PVC hydrodynamic mode.

The analyses in Gupta et al [16, 17] both provided evidence from experiment and linear analysis to explain the role of the centrebody wake in disrupting the PVC. We verify this in this paper by performing a time-windowed network

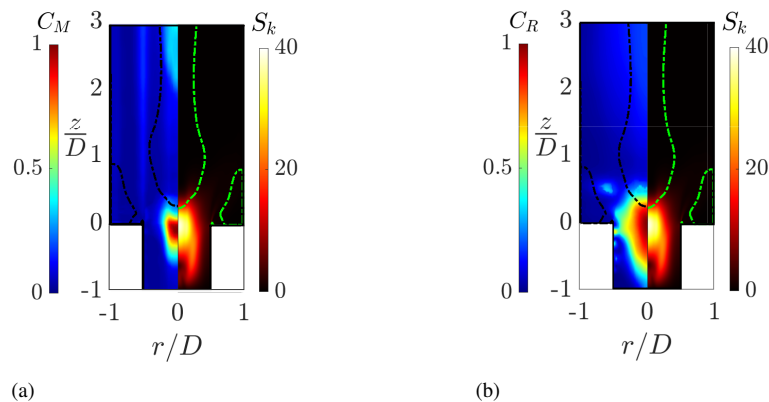


Fig. 9 Wavemaker region for the VBB precession mode identified using (a) normalized weighted closeness centrality using average mutual information ($M_{th} = 0.4$) and structural sensitivity map, (b) normalized weighted closeness centrality using Pearson's correlation ($R_{th} = 0.6$) and structural sensitivity map.

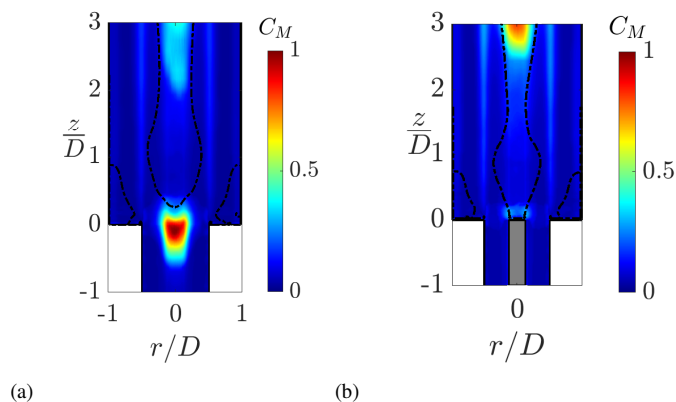


Fig. 10 Normalized weighted closeness centrality based on transverse (radial) velocity time series computed using mutual information with $M_{th} = 0.4$ for (a) case A and (b) case B (refer tab. 1).

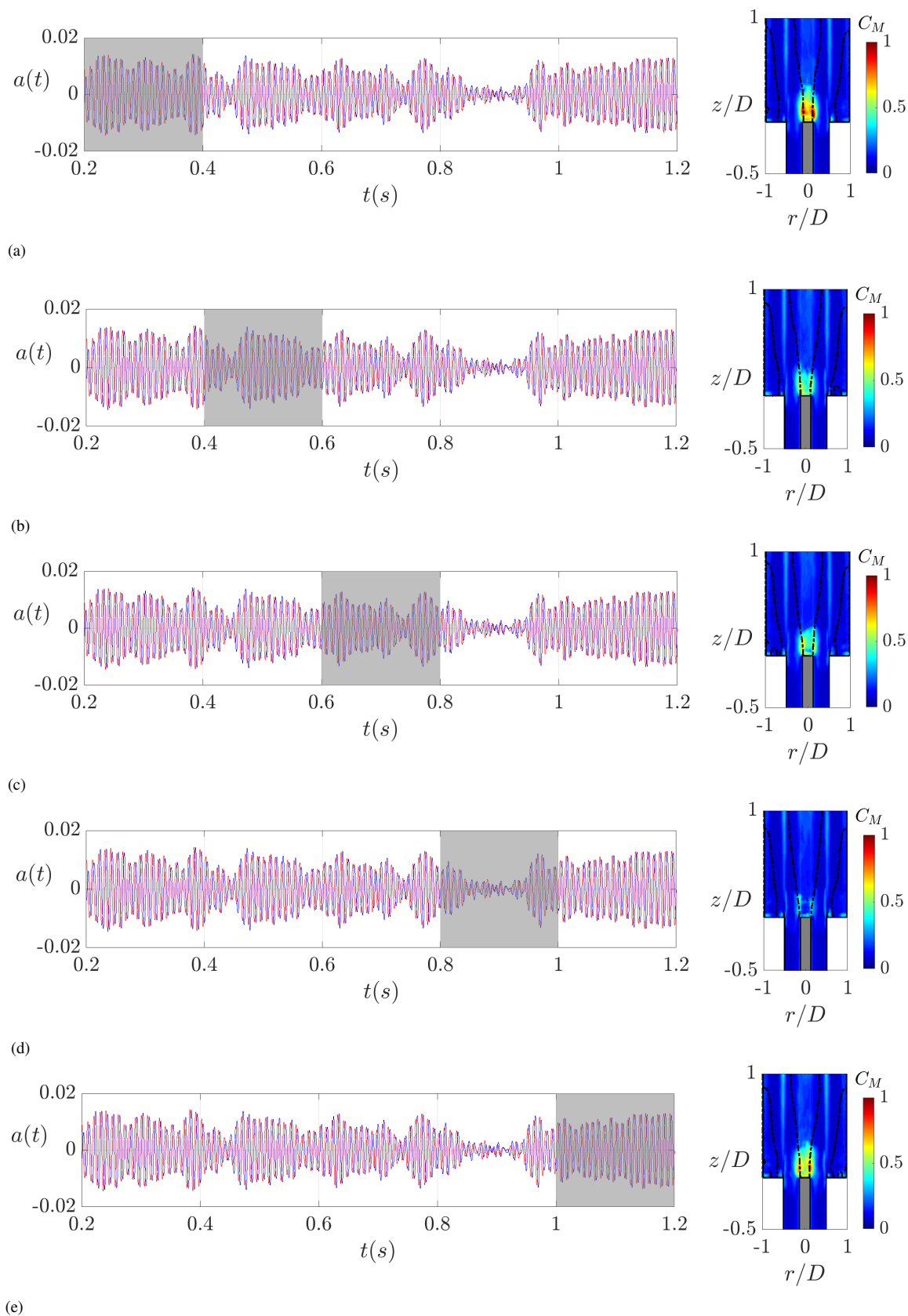


Fig. 11 Time variation of the modal amplitude of the PVC modes determined from LES of case B using WPOD analysis (left) and spatial map of C_i (right) for windowed MI networks obtained for five epochs shown by the gray box on the time series in (a)-(e). A total of 4000 time snapshots were used within each window to construct the network for each case.

analysis using mutual information to determine internode connectivity. The result from this analysis is shown in fig. 11. The time series on the left of each of the figures shows the variation of the amplitude of the two most energetic WPOD (eq. 2) modes determined around the PVC oscillation frequency from the LES data using the procedure described in Gupta et al [17]. The gray box on these time series shows the section of time series data from the LES of case B used to construct the network for that window alone, using the same value of C_{th} as used for the overall network. The corresponding WCC results are shown in each of the figures on the left. During the epoch corresponding to the strong PVC oscillation, in fig. 11a a strong wavemaker is observed in the corresponding WCC result on the right. As the window moves along to the first intermittent disappearance of the PVC (fig. 11b, a corresponding weakening of the PVC wavemaker may be noted in the plot on the right of this figure. This is followed by near complete disappearance, followed by recovery of the wavemaker in figs. 11d and e. This then shows that even though the network constructed with all the data from case B in tab. 1 doesn't show a wavemaker, it does appear during epochs where there is an intermittent PVC oscillation in the flow. This, in turn, is consistent with the fact that due to turbulence fluctuations, an intermittent separation between the centrebody wake and VBB results in intermittent PVC growth as suggested by the experimental study in Gupta et al [17].

VII. Conclusions

This paper presents results that compare two approaches for determining wavemakers, i.e., regions of the flow responsible for the presence of PVC oscillations, in a swirl combustor. These types of analysis aim to provide information that can help guide nozzle design changes that can suppress or promote PVCs. The configuration studied in this paper is a nominally axisymmetric swirl combustor with an axial swirler and a removable cylindrical centrebody [17]. The nominal flow Reynolds number based on nozzle diameter and bulk flow velocity is $Re=20,000$. Our prior study of this flow configuration using LES and linear stability analysis [16] shows the presence of a wavemaker on the centreline, upstream of the vortex breakdown bubble. This result provides an explanation for the suppression of PVC oscillations when a centrebody of appropriate diameter is introduced [17]. We assess the ability of complex network analysis to recover analogous results from time series data alone. The motivation for this is that the time series analysis approach can be applied to flows in complex multi-element configurations and geometries at a cost comparable to that in simpler ones, unlike linear stability. Also, the approach accounts fully for non-linear flow dynamics and for this reason, may be expected to work even when linear theories give incorrect results.

We assess results from two definitions of network connectivity in this paper. The first is the well-known Pearson correlation, and the second is the mutual information between radial velocity fluctuations at nodes corresponding to points within the swirl combustor. Mutual information is a measure of causality between two quantities, even when non-linear interactions govern their dynamics. Formally, it quantifies the reduction in the expectation of the uncertainty in the value of the radial velocity fluctuation at a point, due to the knowledge of velocity fluctuations at another point. We characterize the connectivity of points within the networks constructed thus using the weighted closeness centrality measure [22]. Clusters of nodes also referred to as 'hubs', with high closeness centrality, when mapped into physical space, identify the spatial position and extent of the wavemaker region.

The results show that both correlation and information networks identify wavemaker regions in the flow that are located upstream of the breakdown bubble. They extend upstream into the swirl nozzle. The mutual information network shows a wavemaker region that is more compact when compared to that identified by the correlation network. The spatial extent and position of this region agree more closely with the physics-based structural sensitivity result. As such, these results show that the data-driven complex network analysis does provide analogous insights that physics-based stability analysis provides. The reason for this is the fact that mutual information quantifies causality, even when the relationship between fluctuations at various points in the flow is non-linear. The introduction of a centrebody causes the wavemaker to vanish. However, reconstructing networks in consecutive time windows over an epoch of flow oscillation in which intermittent PVC oscillations are observed, shows that a wavemaker appears and disappears in conjunction with PVC oscillations. Wavemaker insights such as these, obtained using network analysis, serve to provide useful engineering guidance as to where control or passive geometry modification interventions will have optimal impact on the instability that needs to be controlled. Further study in this area needs to be focused on evaluating other information-theoretic causality measures that can serve to identify wavemakers in flows that are more complex than the present single nozzle swirl combustor case.

References

- [1] Hall, M., "Vortex breakdown," *Annual Review of Fluid Mechanics*, Vol. 4, No. 1, 1972, pp. 195–218.
- [2] Leibovich, S., "The structure of vortex breakdown," *Annual Review of Fluid Mechanics*, Vol. 10, No. 1, 1978, pp. 221–246.
- [3] Escudier, M., "Vortex breakdown: observations and explanations," *Progress in Aerospace Sciences*, Vol. 25, No. 2, 1988, pp. 189–229.
- [4] Syred, N., "A review of oscillation mechanisms and the role of the precessing vortex core (PVC) in swirl combustion systems," *Progress in Energy and Combustion Science*, Vol. 32, No. 2, 2006, pp. 93–161.
- [5] Oberleithner, K., Sieber, M., Nayeri, C. N., Paschereit, C. O., Petz, C., Hege, H.-C., Noack, B. R., and Wygnanski, I., "Three-dimensional coherent structures in a swirling jet undergoing vortex breakdown: stability analysis and empirical mode construction," *Journal of Fluid Mechanics*, Vol. 679, 2011, pp. 383–414.
- [6] Manoharan, K., Frederick, M., Clees, S., O'Connor, J., and Hemchandra, S., "A weakly nonlinear analysis of the precessing vortex core oscillation in a variable swirl turbulent round jet," *Journal of Fluid Mechanics*, Vol. 884, 2020, p. A29. <https://doi.org/10.1017/jfm.2019.903>.
- [7] Moeck, J. P., Bourgouin, J.-F., Durox, D., Schuller, T., and Candel, S., "Nonlinear interaction between a precessing vortex core and acoustic oscillations in a turbulent swirling flame," *Combustion and Flame*, Vol. 159, No. 8, 2012, pp. 2650–2668.
- [8] Shanbhogue, S., Sanusi, Y., Taamallah, S., Habib, M., Mokheimer, E., and Ghoniem, A., "Flame macrostructures, combustion instability and extinction strain scaling in swirl-stabilized premixed CH₄/H₂ combustion," *Combustion and Flame*, Vol. 163, 2016, pp. 494–507.
- [9] Mathews, B., Hansford, S., and O'Connor, J., "Impact of swirling flow structure on shear layer vorticity fluctuation mechanisms," *ASME Turbo Expo 2016: Turbomachinery Technical Conference and Exposition*, American Society of Mechanical Engineers, 2016.
- [10] Karmarkar, A., Gupta, S., Boxx, I., Hemchandra, S., and O'Connor, J., "Impact of precessing vortex core dynamics on the thermoacoustic instabilities in a swirl-stabilized combustor," *Journal of Fluid Mechanics*, Vol. 946, 2022, p. A36. <https://doi.org/10.1017/jfm.2022.610>.
- [11] Anacleto, P., Fernandes, E., Heitor, M., and Shtork, S., "Swirl flow structure and flame characteristics in a model lean premixed combustor," *Combustion Science and Technology*, Vol. 175, No. 8, 2003, pp. 1369–1388.
- [12] Escudier, M., and Keller, J., "Recirculation in swirling flow—a manifestation of vortex breakdown," *AIAA journal*, Vol. 23, No. 1, 1985, pp. 111–116.
- [13] Tammisola, O., and Juniper, M. P., "Coherent structures in a swirl injector at Re= 4800 by nonlinear simulations and linear global modes," *Journal of Fluid Mechanics*, Vol. 792, 2016, pp. 620–657.
- [14] Kaiser, T. L., Oberleithner, K., Selle, L., and Poinot, T., "Examining the Effect of Geometry Changes in Industrial Fuel Injection Systems on Hydrodynamic Structures With BiGlobal Linear Stability Analysis," *Journal of Engineering for Gas Turbines and Power*, Vol. 142, No. 1, 2019.
- [15] Mukherjee, A., Muthichur, N., More, C., Gupta, S., and Hemchandra, S., "The Role of the Centerbody Wake On the Precessing Vortex Core Dynamics of a Swirl Nozzle," *Journal of Engineering for Gas Turbines and Power*, 2021. <https://doi.org/10.1115/1.4050155>, URL <https://doi.org/10.1115/1.4050155>.
- [16] Gupta, S., Shanbhogue, S., Ghoniem, A., and Hemchandra, S., "Suppression and Intermittency of Precessing Vortex Core Oscillations in a Swirl Nozzle," *AIAA SCITECH 2023 Forum*, 2023, p. 1061.
- [17] Gupta, S., Shanbhogue, S., Shimura, M., Ghoniem, A. F., and Hemchandra, S., "Impact of a Centrebody On the Unsteady Flow Dynamics of a Swirl Nozzle: Intermittency of PVC Oscillations," *Journal of Engineering for Gas Turbines and Power*, 2021. <https://doi.org/10.1115/1.4052144>, URL <https://doi.org/10.1115/1.4052144>.
- [18] Giannetti, F., and Luchini, P., "Structural sensitivity of the first instability of the cylinder wake," *Journal of Fluid Mechanics*, Vol. 581, 2007, pp. 167–197.
- [19] Gupta, S., Datta, A., Hemchandra, S., and Boxx, I., "Precessing Vortex Core Suppression in a Swirl Stabilized Combustor With Hydrogen Addition," *Turbo Expo: Power for Land, Sea, and Air*, Vol. 86953, American Society of Mechanical Engineers, 2023, p. V03AT04A002.

- [20] Taamallah, S., Shanbhogue, S. J., and Ghoniem, A. F., "Turbulent flame stabilization modes in premixed swirl combustion: Physical mechanism and Karlovitz number-based criterion," *Combustion and Flame*, Vol. 166, 2016, pp. 19–33.
- [21] Krishnan, A., Manikandan, R., Midhun, P. R., Reeja, K. V., Unni, V. R., Sujith, R. I., Marwan, N., and Kurths, J., "Mitigation of oscillatory instability in turbulent reactive flows: A novel approach using complex networks," *EPL (Europhysics Letters)*, Vol. 128, No. 1, 2019, p. 14003. <https://doi.org/10.1209/0295-5075/128/14003>, URL <https://doi.org/10.1209/0295-5075/128/14003>.
- [22] Opsahl, T., Agneessens, F., and Skvoretz, J., "Node centrality in weighted networks: Generalizing degree and shortest paths," *Social Networks*, Vol. 32, No. 3, 2010, pp. 245–251. <https://doi.org/https://doi.org/10.1016/j.socnet.2010.03.006>, URL <https://www.sciencedirect.com/science/article/pii/S0378873310000183>.
- [23] Mathew, J., Lechner, R., Foysi, H., Sesterhenn, J., and Friedrich, R., "An explicit filtering method for large eddy simulation of compressible flows," *Physics of fluids*, Vol. 15, No. 8, 2003, pp. 2279–2289.
- [24] Mathew, J., Foysi, H., and Friedrich, R., "A new approach to LES based on explicit filtering," *International journal of heat and fluid flow*, Vol. 27, No. 4, 2006, pp. 594–602.
- [25] Mathew, J., "Explicit filtering for large eddy simulation as use of a spectral buffer," *arXiv preprint arXiv:1610.01738*, 2016.
- [26] Lele, S. K., "Compact finite difference schemes with spectral-like resolution," *Journal of computational physics*, Vol. 103, No. 1, 1992, pp. 16–42.
- [27] Datta, A., Mathew, J., and Hemchandra, S., "The explicit filtering method for large eddy simulations of a turbulent premixed flame," *Combustion and Flame*, Vol. 237, 2022, p. 111862. <https://doi.org/https://doi.org/10.1016/j.combustflame.2021.111862>, URL <https://www.sciencedirect.com/science/article/pii/S0010218021006052>.
- [28] Carpenter, M. H., Gottlieb, D., and Abarbanel, S., "Time-stable boundary conditions for finite-difference schemes solving hyperbolic systems: methodology and application to high-order compact schemes," *Journal of Computational Physics*, Vol. 111, No. 2, 1994, pp. 220–236.
- [29] Poinso, T. J., and Lele, S. K., "Boundary conditions for direct simulations of compressible viscous flows," *Journal of computational physics*, Vol. 101, No. 1, 1992, pp. 104–129.
- [30] Towne, A., Schmidt, O. T., and Colonius, T., "Spectral proper orthogonal decomposition and its relationship to dynamic mode decomposition and resolvent analysis," *Journal of Fluid Mechanics*, Vol. 847, 2018, pp. 821–867.
- [31] Pope, S. B., *Turbulent Flows*, Cambridge University Press, 2000. <https://doi.org/10.1017/CBO9781316179475>.
- [32] Reynolds, W. C., and Hussain, A. K. M. F., "The mechanics of an organized wave in turbulent shear flow. Part 3. Theoretical models and comparisons with experiments," *Journal of Fluid Mechanics*, Vol. 54, No. 2, 1972, p. 263–288. <https://doi.org/10.1017/S0022112072000679>.
- [33] Hecht, F., "New development in FreeFem++," *J. Numer. Math.*, Vol. 20, No. 3-4, 2012, pp. 251–265. URL <https://freefem.org/>.
- [34] Juniper, M. P., and Pier, B., "The structural sensitivity of open shear flows calculated with a local stability analysis," *European Journal of Mechanics-B/Fluids*, Vol. 49, 2015, pp. 426–437.
- [35] Barrat, A., Barthelemy, M., Pastor-Satorras, R., and Vespignani, A., "The architecture of complex weighted networks," *Proceedings of the national academy of sciences*, Vol. 101, No. 11, 2004, pp. 3747–3752.
- [36] Green, D. G., "Emergence in complex networks of simple agents," *Journal of Economic Interaction and Coordination*, 2023, pp. 1–44.
- [37] Taira, K., and Nair, A. G., "Network-based analysis of fluid flows: Progress and outlook," *Progress in Aerospace Sciences*, Vol. 131, 2022, p. 100823.
- [38] Cover, T. M., *Elements of information theory*, John Wiley & Sons, 1999.
- [39] Shannon, C. E., "A mathematical theory of communication," *The Bell system technical journal*, Vol. 27, No. 3, 1948, pp. 379–423.
- [40] Li, W., "Mutual information functions versus correlation functions," *Journal of statistical physics*, Vol. 60, 1990, pp. 823–837.
- [41] Donges, J. F., Zou, Y., Marwan, N., and Kurths, J., "Complex networks in climate dynamics: Comparing linear and nonlinear network construction methods," *The European Physical Journal Special Topics*, Vol. 174, No. 1, 2009, pp. 157–179.

- [42] Lüdtke, N., Panzeri, S., Brown, M., Broomhead, D. S., Knowles, J., Montemurro, M. A., and Kell, D. B., “Information-theoretic sensitivity analysis: a general method for credit assignment in complex networks,” *Journal of The Royal Society Interface*, Vol. 5, No. 19, 2008, pp. 223–235.
- [43] Barabási, A.-L., and Albert, R., “Emergence of Scaling in Random Networks,” *Science*, Vol. 286, No. 5439, 1999, pp. 509–512. <https://doi.org/10.1126/science.286.5439.509>, URL <https://www.science.org/doi/abs/10.1126/science.286.5439.509>.
- [44] Watts, D. J., and Strogatz, S. H., “Collective dynamics of ‘small-world’ networks,” *nature*, Vol. 393, No. 6684, 1998, pp. 440–442.
- [45] Das, R., and Porfiri, M., “A controlled transfer entropy approach to detect asymmetric interactions in heterogeneous systems,” *Journal of Physics: Complexity*, Vol. 4, No. 2, 2023, p. 025020. <https://doi.org/10.1088/2632-072X/acde2d>, URL <https://dx.doi.org/10.1088/2632-072X/acde2d>.